UNIVERSITY OF CALIFORNIA,
IRVINE

Oxygenation of Implantable Tissue Using Microbubble Technology

THESIS

submitted in partial satisfaction of the requirements
for the degree of

MASTER OF SCIENCE

in Biomedical Engineering

by

Kenneth Campos

Thesis Committee:
Assistant Professor Mark Bachman, Chair
Professor Guann-pyng Li
Professor William Tang

2015

Figure 1: Bubble Characteristics © 2015 Pan Stanford Publishing

DEDICATION

To

Barbara and Ken Campos
Antonio Luna

In recognition of their worth

Thank you for always believing in me and for your continued support throughout my life. I am truly blessed and thankful to have such wonderful influences in my life

TABLE OF CONTENTS

LIST OF TABLE AND FIGURES

ACKNOWLEDGMENTS

I would like to express the deepest appreciation to my committee chair, Mark Bachman, who took the time to direct me in pursuit of my graduate degree.

I would like to thank my committee members, Professor Guann-pyng Li and Professor William Tang, for their support throughout my thesis

In addition, I would like to thank Dr. Alan Widgerow and Derek Banyard without their guidance and persistent help this project would not have been possible

A special thanks to Mike Klopfer for all his hard work he put into the lab his guidance, and his willingness to assist wherever possible. Some of the information presented in this thesis is duplicated in his report.

I thank Pan-Stanford Publishing for permission to include copyrighted photographs as part of my thesis/dissertation. I also thank YSI Incorporated and Milwaukee Instruments for permission to include documents and images regarding their oxygen probes

ABSTRACT OF THE THESIS

Oxygenation of Implantable Tissue Using Microbubble Technology

By

Kenneth Ronald Campos

Master of Science in Biomedical Engineering

University of California, Irvine, 2015

Assistant Professor Mark Bachman, Chair

[Adipose tissue grafting is quickly becoming a common practice in plastic surgery. The recent discovery that adipose tissue contains stem cells has also fueled substantial interest in the technique for regenerative medicine. However issues with necrosis and variability of graft retention have remained problematic. Cell death occurs due to lack of nutrients, with oxygen being the most vital. Studies have shown that adipose tissue can only survive up to 3 days in hypoxic conditions. The success of an adipose graft is a race between angiogenesis and cell fitness under hypoxia. Current methods to address necrosis focus on harvesting and preparing cells to have a high survival rate in hypoxic conditions. We believe that bathing the tissue graft in a microbubble solution will enhance its viability over time. The nanobubbles function as an initial reservoir of additional oxygen for the cells to take up as needed. In addition, these nanobubbles can also activate several processes responsible for angiogenesis, and general cell function. In our lab, we have created an efficient device that can deliver gas micro and nanobubbles into solution. We feel that in combination with this device, we can quickly and efficiently increase graft viability and future graft retention over time. The addition of microbubbles during processing, provides a measurable reduction in the time cells spend under hypoxic conditions and thus increase the survival rate of cells and the retention rate of grafts]

INTRODUCTION

Adipose tissue grafts have seen a dramatic increase in usage as people investigate their characteristics and potential uses. One potential use for these tissue grafts is for regeneration of injuries. Grafts can be processed to create a regenerative mixture that includes adipose derived stem cells (ADSCs). Since the mixture is derived from adipose tissue, they can be extracted from a patient, processed, and re-injected as an autologous tissue graft. The therapy suffers from drawbacks that need to be addressed before it can see widespread clinical use. These include unpredictable retention rates and necrosis. Implanted grafts containing ADSCs retain anywhere from 20-80% of their initial volume over the course of a few months[1]. Recent studies have focused on harvesting and implantation techniques to limit the amount of necrosis. A tissue graft procedure has several factors that must be balanced in order to be successful. The most important details of this environment involve the availability of oxygen.

In the initial phases of tissue growth, oxygen availability is extremely important for cell survival. Studies have shown that a hypoxic environment inhibits the growth rate of cells. In hypoxic conditions (around 1% oxygen partial pressure), the normal growth of cells is reduced to approximately one-third the normal levels. When exposed to long term hypoxic conditions, cells are directed along the apoptosis pathway and approximately 80% of cells die within 48 hours of prolonged exposure. This timeframe is particularly important because angiogenesis does not occur until around 48-72 hours after transplantation. Extremely high oxygen conditions (above 30% atmospheric value) has cytotoxic effects on the cells causing a region of dead tissue and necrosis over time. However, levels in between standard atmospheric oxygen tension and below the cytotoxic range (100%-130% atmospheric oxygen tension) promote angiogenesis within tissue culture[2]. In the initial environment surrounding the tissue post-implantation, there are

several additional factors to balance. The oxygen tension at any point in the tissue can be estimated by the amount available from the surrounding environment (source), additional supply available due to transport, and the amount of oxygen consumed by the tissue. However, the growth of the tissue and onset of angiogenesis, requires a steady oxygen supply to maintain the energy necessary to the cells. Cells require more energy to repair their internal structure and connect to the surrounding region of implantation. Therefore, the local oxygen supply is strained, which makes the graft highly susceptible to hypoxic conditions. Typically, this steady oxygen supply would be available through transport from the capillaries and other vessels surrounding the region. However, these vessels are non-existent until a couple days have passed. Therefore, the oxygen supply must be maintained through the local oxygen tension itself, which is primarily transported via diffusion. The simplified 1-D diffusion case is shown below for illustration:

$$\frac{\partial c(x,t)}{\partial t} = D\frac{\partial^2 c(x,t)}{\partial x^2}$$

As shown in the equation, the diffusion force is dependent on the oxygen gradient of the environment and the travel distance from the source. In the case of the implantable graft, this source is primarily the blood vessels once angiogenesis occurs.

According to recent studies, the size of implanted tissue is severely limited by the rate of diffusion into the tissue. This critical value is estimated to be around .16 cm in radius. Above this value, the cells at the center of the graft are unable to maintain the minimum oxygen supply for survival and undergo apoptosis as a result. Eventually this region becomes a necrotic core in which all the cells die off. Since most procedures require a graft larger than this size, it is often recommended to insert the required volume as several small boluses smaller than .16 cm in radius rather than 1 large bolus of the necessary size. In addition, the pressure of the

compartment must be kept relatively low so as not to block fluid flow through the compartment. The critical pressure for the compartment occurs around 9 mmHg. Above this value, fluid flow becomes severely limited, and the graft becomes more hindered[1,3].

Taking into account all of these factors, a solution to these issues would have to account for several characteristics. The proposed solution must help bridge gap between graft processing/implantation and angiogenesis. Therefore, the additional system must be relatively stable and either last for a few days, or its effects must continue through this time point at minimum. Since oxygen is the limiting factor in graft retention, we chose oxygen as our main target with the goal to provide tissue with an additional oxygen source from which to draw upon. However, the system must be maintained such that it stays below cytotoxic levels. To ensure, the alternative did not rise above this threshold, we chose a target of 125% of atmospheric oxygen levels. We also wanted to provide a device in a cheap and efficient form to deliver the oxygen supply with the future application of clinical use.

MICROBUBBLES

Background Information

Through research, it was found that a micro/nanobubble system could be an interesting addition to the tissue grafting story and their properties would create a possible advantage over the general case. Over the years, manufacturer and industrial interest has been growing towards various applications for micro/nanobubble technology, primarily in Japan and the surrounding regions. Interest in this area have been mostly focused on the flocculation and cleaning aspects of microbubbles. This has led to their use in wastewater cleanup, brewing and environmental remediation. Eventually this interest shifted to more consumer-friendly applications like pet grooming, shower head modifications, and other cleaning based uses. Currently there are limited

products aimed at biomedical applications. However it is plausible to harness their physical properties to clean a wound or tissue area while providing a reservoir of additional oxygen to prevent long-term hypoxia.

In order to explain the use of micro/nanobubbles in a biomedical application, it is first necessary to define their behavior. Bubbles in general can be classified into three main categories: Macrobubbles, microbubbles, and nanobubbles. Each of these bubble types have their own characteristics and uses. Macrobubbles are defined as bubbles that are larger than 100 microns in diameter. Bubbles of this size are the general form that are created via soap bubbles or vigorous shaking and encountered in everyday life. These bubbles are visible to the unaided eye and are thus easily observable. At this size, bubbles have short-term stability and when immersed in a solution, they will quickly rise to the surface and burst. This popping occurs due to a rapid expansion that occurs from reduced hydrostatic pressure as the bubbles rise. Due to their short-term stability they were not chosen to be the focus of this report. Microbubbles, however, are typically classified as bubbles with radii between 1 and 100 microns. At this smaller size, the microbubbles also have the ability to rise or shrink in solution, however, they are slower to rise due to additional stability which allows them to remain in solution for a longer period. In solution they appear as a cloudy solution but are not individually distinguishable without magnification. Smaller than 1 micron, bubbles are classified as nanobubbles. Nanobubbles, themselves, are difficult to observe through normal techniques and require the use of additional methods such as laser backscatter or dynamic laser scattering measurements. This classification of bubbles have a further increased stability which allows them to survive for several days or longer under ideal conditions[4].

Microbubble Properties

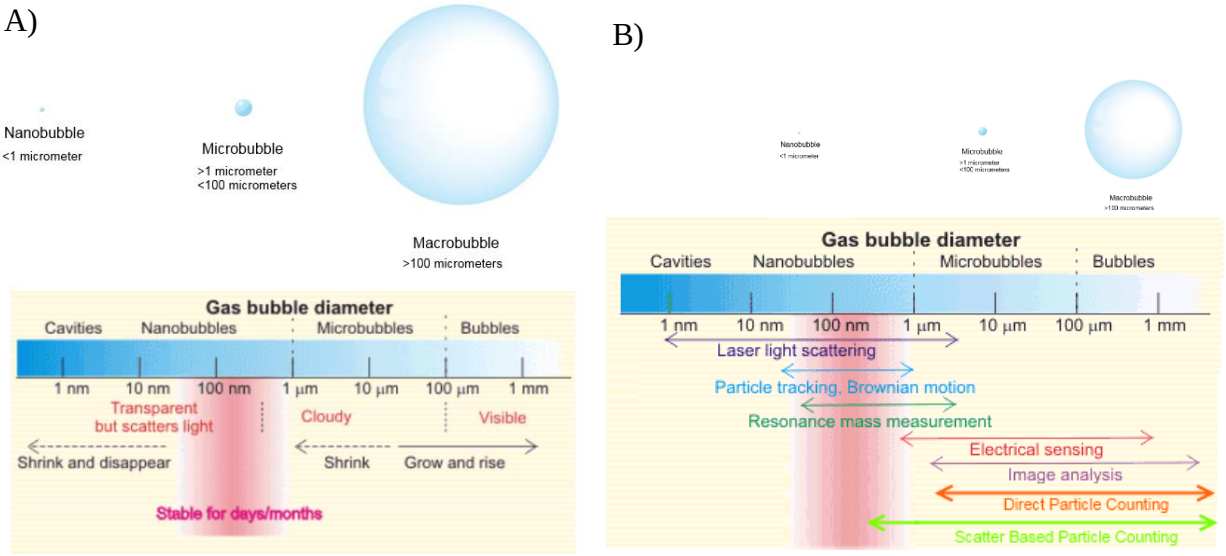

Figure 1 Bubble Characteristics: (A) Bubble behavior and observable properties in solution as a function of diameter, (B) Typical measurement techniques and range of evaluation for each bubble size[4]. Figure reproduced in modified form with express permission from Pan Stanford Publishing

The shrinking of microbubbles can be modeled in a simplified form by the Young-Laplace relationship. This model relates the change in pressure inside and outside of a trapped gas sphere as a function of the sphere's diameter and the interfacial surface tension.

$$\Delta P = \frac{4\sigma}{d} \quad \textit{Equation 1}$$

As the diameter (d) decreases, the trans-interface pressure (ΔP) increases as the surface tension (σ) remains constant [$\sigma_{Water\text{-}Air} \approx 72.8$mN/m @ 20°C]. As microbubbles shrink in size a dynamic equilibrium is eventually reached where the contractile force is balanced against internal pressure. As the bubble size decreases it experiences larger pressures under this model. For example: a nanobubble around 1 µm in diameter would have an internal pressure of 2 atm, and a microbubble around 100 nm bubble in size will have an internal pressure of about 15 atm.

As the bubbles shrink and disappear their contents are dispersed into the local environment. A simplified conceptual model for gas delivery via microbubbles can be explained by coupling the internal gas pressure of the bubbles with Henry's law. The pressure of the gas (within the local area) in reference to the pressure of the liquid is proportional to the dissolved concentration of the gas. High internal bubble pressures result in local diffusion of gas into liquid. As local dissolved gas concentration increases, a dynamic equilibrium is reached at saturation. The bubbles serve as an additional area to contain the excess gas molecules until the contents can be delivered into some other area. Bubbles individually can thus expand or contract to maintain this equilibrium. This model is plausible and has been widely reported, but when one considers the solution open to the atmosphere (a container of relatively infinite size), the equilibrium will continue to shift towards atmospheric saturation, the nanobubbles would shrink and disappear rapidly. The lifetime of nanobubbles experimentally are substantially longer than predicted by this model. To date, a comprehensive model explaining nanobubble properties and lifetime has not been created although many of their properties are known. Reports by Attard in addition to Petsev et. al in discuss the evolution of modeling nanobubble equilibrium in substantial depth[5,6]. This report is focused on the clinical applications of bubbles specifically directed at the improvement of autologous fat grafts.

The biologically pertinent properties of micro and nanobubbles are summarized below:

- As the internal pressure is increased, the pressurized gas is a driving force for gas delivery in liquid. High super-saturation levels can be produced with microbubbles in water. Nanobubbles can dynamically release and absorb gas in solution acting as gas reservoirs.

- The rapid adiabatic compression of gas can lead to elevated temperatures in the localized region. The magnitude of the absolute temperature of microbubble collapsing is debated[4].
- Radicals are produced during the collapse of microbubbles. Li and Takahashi demonstrated catalytic oxidation of phenol in the presence of a copper catalyst in an acidic environment[7]. The mechanism is believed to arise from the production of hydroxyl radicals in solution (·OH)[4,8,9], the scavenging of hydroxyl radicals by tert-butyl alcohol and the rate of phenol degradation.
- Microbubbles have demonstrated the ability to efficiently flocculate particulates or suspend oil/grease in water[10]. Microbubble generation systems have been used in wastewater separation systems separating both solid and liquid components
- Microbubbles have shown the capability for surface cleaning[11–13]. New approaches have investigated nanobubbles produced by alternative methods such as shear and pressurization of gas and solution mixtures
- Microbubbles are not limited to gas alone, depending on the method of manufacture and the contents they are exposed to, microbubbles can theoretically be made to include any number of liquids and gases. This has the potential to be used for both directed gas and drug delivery mechanisms in the future.
- Microbubbles have been shown to promote growth in aquaculture[15] . While microbubbled water is correlated with the growth of plant and animal life, it is unknown whether the process stimulates nutrient uptake or directly affects growth.

Additionally different species react in different ways to microbubble water. Some studies have hinted at the bactericidal properties of nanobubble solutions, however the underlying cause is unknown. Efficient fluid flow, oxygenation, or microbubble surface properties may be possible explanations for this biological interaction. It is possible that the ionic charges on the surface of a microbubble, allow the breakdown of specific bonds or that the flocculation of particles functions as an additional filtration process. Even with the short lifetime, breakdown of pathogenic agents in the water column may lead to improved growth.

Investigations into the fluid dynamics of microbubble generation and flow have been investigated to a moderate extent on an academic level. Interest for practical microbubble applications has been growing in recent years. Much of this research is centered in Japan and Korea. Firms from these countries have produced a number of industrial products for flocculation, aeration, and environmental remediation. Several other companies have included microbubble technology in consumer products such as faucet taps and shower heads. Additionally, complete microbubble systems for pet grooming and hair care have been patented or are in production. Many of these manufacturers market their products as a type of panacea that can various applications ranging from deep pore cleansing and boosted cleaning with detergent, or even detergent less cleaning. Therefore, it is important to separate scientific truth from claims for microbubble technology. Despite many unsubstantiated and exaggerated marketing claims, microbubbles exhibit clear cleaning and oxygenation effects. Many properties are unique to the nanobubble system alone as they show promise as an alternative to specific cleaning products or can be used an additional level of functionality.

Microbubble Generation

A variety of products on the market advertise microbubble generation as their output. However, through our research only certain types of microbubbles were able to persist and deliver oxygen into a solution. Certain types of generators that focus on methods such as shear forces to create their nanobubbles are weak methods to trap a reserve of oxygen within solution. Additionally, forcing solution through a nozzle is not sufficient enough to produce a sufficient concentration of microbubbles that can effectively deliver oxygen. Certain industrial style pumps such as the Nikuni pump function well to create microbubbles of the correct size and properties, however, they are prohibitively expensive to use in a normal setting. For our purposes, we set out to create a more cost-effective method of generating micro and nanobubbles that could create bubbles of the desired properties while maintaining a low-end cost. To achieve our goal, we finally settled on the following simplified prototype version. The most important part of this device is the gear pump and pressure valves that were chosen. They were both chosen for their ability to withstand high pressures while still maintaining function.

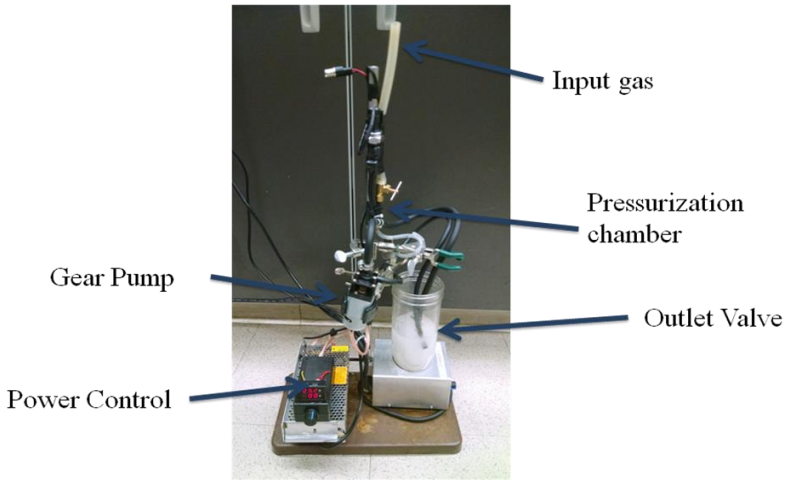

Figure 2 Micro/Nanobubble Generation Device: Simple system created to generate microbubble solution for low-scale experiments. The device forms gas microbubbles and combines them under pressure into a liquid solution

This machine is primarily controlled through a variable power supply unit located near the base. The device works by utilizing a simple gear pump in combination with a pressurization system to generate the micro/nanobubble solution. Two inputs are required for useful operation. In the illustrated setup, input gas (air in this case) is combined under pressure with liquid distilled water. This pressure and flow rate into the chamber can be controlled via knobs attached to the system. Additionally, if desired, the pressure can also be monitored via an attached gauge on the side. This gauge outputs a voltage value that can then be converted to the pressure reading inside the pressure chamber. After pressurization the liquid/gas mixture then flows out through rubber tubing into a nozzle for delivery into the bulk solution. In Figure 2, this bulk solution is then drawn back into the device, where it is chopped into minute pieces using the gear pump. Once cut into smaller pieces, the liquid is then recombined with additional gas and then redelivered into the bulk solution. After a few cycles, the result is a thick microbubble solution as demonstrated in the figure below (Figure 3)

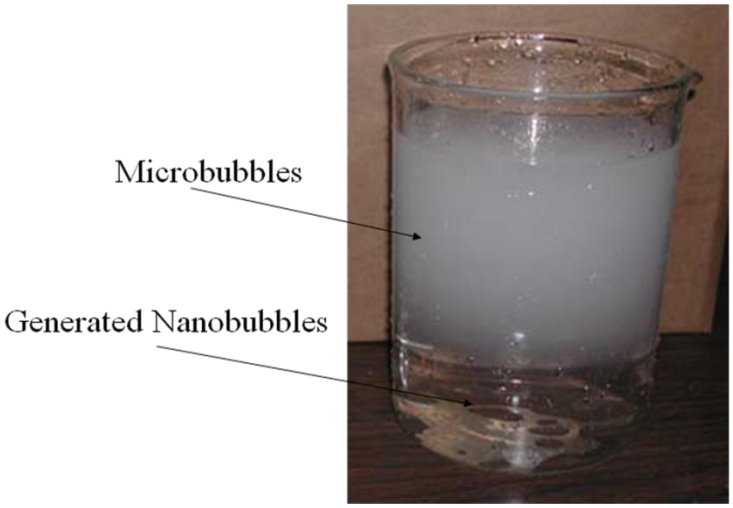

Figure 3: Example of Observable Micro/Nanobubbles in DI water Solution: Microbubbles initially appear as a milky white substance in solution. Over time, the bubbles shrink and eventually become invisible to the naked eye. At the nanobubble scale, the bubbles are still detectable through laser light scattering.

The resultant microbubbles contained within the water, start out at larger sizes but after several cycles they reach an initial size around 30 microns in diameter. However, these microbubbles shrink over time, such that, they deliver their gas contents into solution. Some of these microbubbles hit an equilibrium point around 1 micron in radius where they persist in solution for long periods of time as shown in Figure (3). At the nanobubble level, they are invisible to standard detection and most particle counters and can only be detected through alternative methods such as laser light scattering[4]. The distribution of the generated microbubbles and their shrinking behavior is illustrated further in Figure 4.

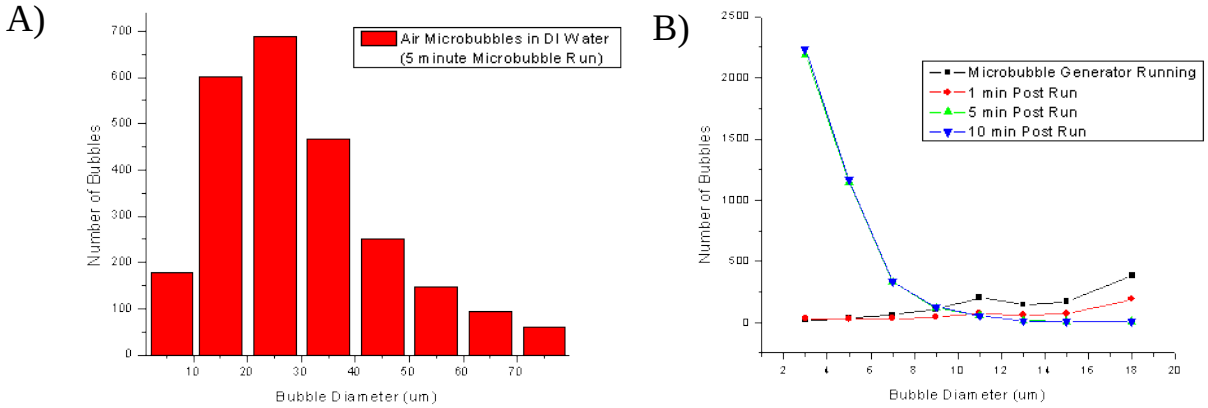

Figure 4 Particle Counter Data: (A) Initial microbubble distribution following 5 min generation time. (B) Bubble size over time. Bubble initially start at around 25 microns in diameter. Over time the bubbles shrink in solution to approximately 2 microns or less

These microbubbles also function as a reservoir for additional oxygen to be maintained locally within the solution. A noticeable increase in oxygen occurs even when using air as the gas source. This increase is measurable via both standard Clark electrode and through Winkler titration. After a running time of approximately three minutes, the liquid solution is oversaturated with additional oxygen and reaches a new maximum value that can be maintained through continuous use of the pump device.

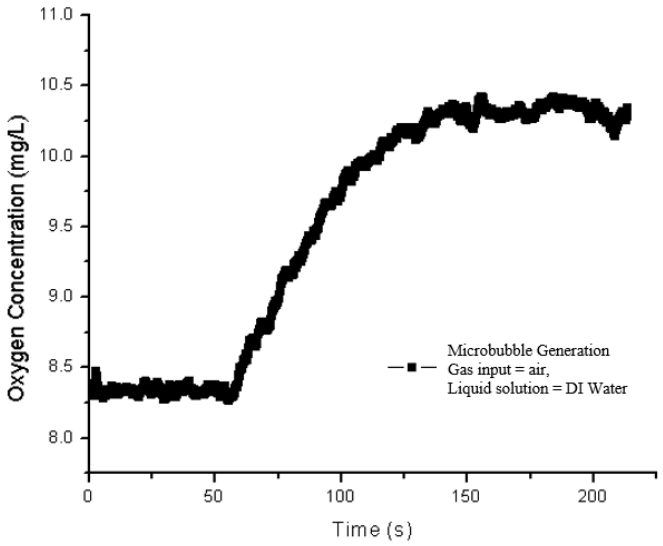

Figure 5: Performance of Microbubble Generator Device. Microbubble generation using air as gas input and water as the liquid solution. Dissolved oxygen measurements rise after initial device usage until maximum value is reached at a new threshold.

MEASUREMENT OF OXYGEN VIA CHEMICAL METHODS

Winkler titration test:

The Winkler titration method is a well-documented assay to determine the oxygen concentration of a solution. It is frequently used in environmental studies that require estimates of water quality to determine the health of wildlife. This analytical test is used to determine the oxygen concentration of a solution. This method first was developed by Lajos Winkler in 1888[16]. The original method is still in use today with minor improvements for accuracy[17–19]. This process involves the addition of specific compounds (manganese, iodide, and hydroxide) is added to a liquid sample of interest in order to convert the dissolved oxygen into a more easily measured state. In our tests the liquid sample of interest most often corresponded to water or PBS with varying degrees of dissolved oxygen.

Standard Procedure and Reactions Involved

60 mL of sample solution is added to a 60 mL Biological Oxygen Demand (BOD) bottle and a glass stopper is added to contain the sample. Careful procedures must be taken at this point to eliminate any air bubbles that form. Any trapped air bubbles that form at this point will interfere with the final concentration reading, and creates additional error by adding extra oxygen to the system which raises the measurement value.

[STEP 1: Addition of Manganous Sulfate] Manganous Sulfate is then added to the sample solution followed by the addition of lithium hydroxide (strong alkali) to make divalent manganese hydroxide ($Mn(OH)_2, white\ solid$). The reaction of Mn^{2+} and hydroxide leads to the precipitation of $Mn(OH)_2(s)$. The reaction occurs under the assumptions that $Mn(OH)_2(s)$ has enough solubility in a basic environment such that Mn^{2+} ions are present in solution to perform reactions and the $Mn(OH)_2(s)$ acts as a reservoir for Mn^{2+} ions.

[STEP 2: Manganic Hydroxide Equilibrium] The oxygen present in the solution reacts with the Mn^{2+} ions to oxidize them to Mn^{3+} ions. The Mn^{3+} ions oxygen in the basic solution reacts with the $Mn(OH)_2$, resulting in precipitation of brown manganic hydroxide ($MnO(OH)_2(s)$). At this point the oxygen in solution acts as the limiting agent and the proportion of manganic hydroxide generated is related stoichiometrically to the original amount of oxygen present in the solution.

[STEP 3: Oxidation of Iodide] The solution is then acidified. At this point the Mn^{3+} ions react with the iodide present in the solution to convert the iodide into iodine. The Mn^{3+} ions in the acidic environment are reduced to Mn^{2+} ions while oxidizing the iodide into iodine. Once the procedure has reached this point, the solution is considered fixed. The reagent mixture has no appreciable reactionary sensitivity to oxygen.

[IODINE-TRIIODIDE EQN] The generated iodine (I_2) and residual iodide (I^-) forms an equilibrium with the triiodide ion (I_3^-). The triiodide ion acts as a reservoir for iodine in solution. The iodine and especially the triiodide appear as a visible brown color in solution.

[Step 4: Titration with Standardized Thiosulfate Solution] A thiosulfate solution is used to titrate the iodine back into colorless iodide. The thiosulfate oxidizes iodine (limiting both the I_2 and I_3^- concentrations in solution) to iodide while the thiosulfate is reduced to tetrathionate. As iodine is converted to iodide the color shifts from brown to clear. The equivalency point (when the solution becomes clear) for the iodine is proportional to the original oxygen content of the solution tested.

Shown below are the main reactions in each step of the Winkler titration test:

$$Mn^{+2} + 2OH^- \rightarrow Mn(OH)_2 \qquad \text{Step 1}$$

$$2Mn(OH)_2 + \frac{1}{2}O_2 + H_2O \rightarrow 2MnO(OH)_2 \qquad \text{Step 2}$$

$$2Mn(OH)_3 + 2I^- + 6H^+ \rightarrow 2Mn^{+2} + I_2 + 6H_2O \qquad \text{Step 3}$$

$$I_2 + I^- \leftrightarrow I_3^- \qquad \text{Iodine-Triiodide Eq.}$$

$$I_3^- + 2S_2O_3^{-2} \rightarrow 3I^- + S_4O_6^{-2} \qquad \text{Step 4}$$

The triiodide ion (I_3^-) is the major colorant in the solution. The major absorption for this species is between 350 and 500 nanometers. Several modifications are made in the procedure to aid in precision determination of equivalency. Literature suggests that a starch solution can be added in addition to the thiosulfate to amplify the color change from brown to clear. The starch reacts with the iodine and especially the triiodide ions in solution to form a blue-black colored complex which is easier to distinguish with the naked eye. Alternatively a solution of sodium EDTA can be used instead of iodine as a pink complex is formed with manganese[20]. We have found in our studies that absorbance can be measured via spectrophotometer to alternatively find

the equivalency point. With the addition of spectrophotometer, additional colorimetric chemicals are unnecessary.

Nitrite Interference within the Winkler Method

Several competing ions can change the result of the test specifically nitrites are problematic. The accuracy of the original Winkler procedure is severely limited by the amount of nitrites present. Nitrites interfere with the chemical reactions that take place and reduce the accuracy of the measurement. The higher the concentration of nitrites within the sample, the less accurate the test becomes 12.6 % error at 5mg nitrite per liter sample at low oxygen concentrations[21]. To lessen the nitrite interference, sodium azide is added to the solution to reduce the nitrite in the acidic final environment as represented by the chemical equation. (>.1 mg/L of nitrous acid)

$$\boldsymbol{N_3^- + H^+ \rightarrow NH_3 + NO_2^- + H^+ \rightarrow N_2 + N_20 + H_20}$$

The azide modification drastically reduces the effects of nitrites on the final measurement such that the nitrites do not have an appreciable impact on the measurement[21].

Calibration of Winkler Kit Procedure (manufacturer version)

Evaluation of Equivalency Point via Eye Threshold

Calibration of this process is achieved by determining a relationship between the volume of titrant added and a reference value for this substance. In this particular situation iodine is titrated by thiosulfate to determine the content of oxygen in the original sample. So the relation of interest is the proportionality of thiosulfate to oxygen. The chemistry set used for this analysis was a Hach Model OX-2P. Per the instructions given, the number of drops added of thiosulfate were each equivalent to neutralizing 1 mg/L of oxygen. If 10 drops is used to neutralize the iodine content, than the original solution contained 10 mg/L of oxygen. However, this leads to an inherent error of about 0.5 mg/L in the final measurement. By modifying the concentration of

the experimental solution relative to the drop size, the equivalent value (in mg/L) of oxygen that each drop represents can be reduced, leading to greater precision. Several assumptions are made with this kit. Firstly, the drop size must be identical to maintain analytical precision across the titration. The manufacturer indicates that the drop size from the kit corresponds between 14.5 to 15.5 drops/mL per their internal certification (exp Apr. 2009). Secondly the titration concentration of the thiosulfate must be exact. The manufacturer certified the concentration is stabilized to remain at 0.0109 N normalcy. No tolerance value was specified by the manufacturer in their certifications. The identification of the equivalence point was to be performed by visual identification of a clear test tube against a white card. Titration was ceased when the tube became subjectively clear.

In analysis of the construction of this kit, the end point, however, is subjective. There is no rapid shift as classically observed in a phenolphthalein, instead a gradual color change is observed which results in a less detectable endpoint by eye. A subjective test was performed to evaluate where the eye observed colorless point was with respect to the kit.

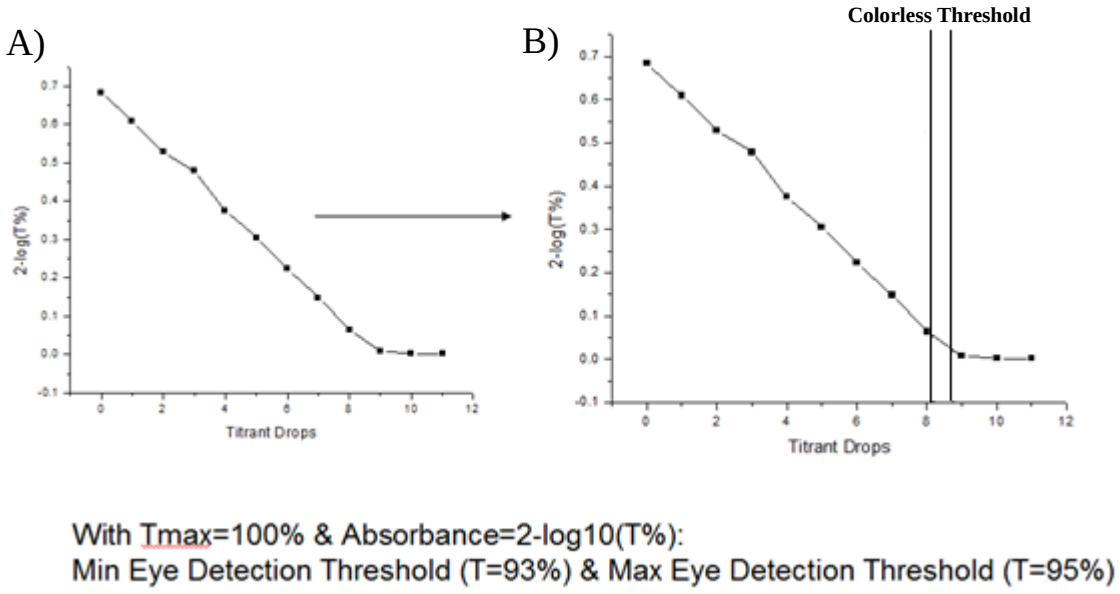

Figure 6: Analysis of Winkler Titration Kit. (A)Initial Data, (B) Eye threshold range. Standard kits provide an estimate of dissolved oxygen content of liquid solutions but are met with consistency issues that stem from its reliance on a human observer. This measurement value can vary from operator to operator or even day to day

Based on a number of tests, it was clear that the true equivalence point was not observed by eye. After 5 tests, with two observers, it was concluded that the visually observed equivalency point corresponded to approximately a transmission of 93% to 95% as determined by the spectrophotometer. This number varied from operator to operator and therefore could only determine a window of equivalency through the use of large incremental values. The actual equivalency point as determined by the spectrometer was consistently higher than the value determined through the unaided eye. Accordingly the solution would be concluded, by eye, as over-titrated. According to the manufacturer, the kit was designed for eye based titration and the reagent concentrations adjusted accordingly. For this reason, we took the system a step further to ensure accurate measurement of each sample.

Accurate Determination of Equivalency Point

Colorimetric additions and eye determination was eliminated for these experiments through the use of device measurements (spectrophotometer). As the concentration of iodine is reduced in solution, the solution shifts proportionally from brown to colorless. The transition in color was assumed to follow a standard Beer-Lambert law model[22]. As the concentration of iodine is reduced (converted to colorless iodide), the absorption reduces in the 350-500 nanometer color range. This relationship is expressed as follows:

$$C = \frac{A}{\varepsilon \cdot L} \quad \textit{Equation 2}$$

$$A = \log_{10}(\frac{I_O}{I}) = \log_{10}(\frac{\%T_O}{\%T}) = \log_{10}(\%T_O) - \log_{10}(\%T) \quad \textit{Equation 3}$$

Where A is absorption value, ε is the molar extinction coefficient, and L is the optical path length, I_O is the incident photon number, I is the measured photon number, $\%T_O$ is the maximum transmittance of the sample (typically set to 100%), and %T is the spectrophotometer measured optical count percent.

In practical use, for a simple spectrophotometer the following relationship is used:

$$A = \log_{10}(\%T_O) - \log_{10}(\%T) \quad \textit{Equation 4}$$

This is due to the fact that the maximum photon measurement is manually set to be 100% transmission. In special circumstances this value may change, in which case the first term can be recalculated independently. For 100% incident transmission, this form simplifies down to the following:

$$A = 2 - \log_{10}(\%T) \quad \textit{Equation 5}$$

Once the transmission values are converted to absorption values, the addition of titrant is generally linear with respect to absorbance. If the absorption or concentration is too high in the

sample, the instrument may not have sufficient dynamic range to detect linear shifts on the high absorbance end. Likewise, if the concentration is very low, the instrument may be unable to detect small concentration changes at the low end as well. To combat this in a practical situation, several techniques must be applied. Firstly, the instrument must have linear response (absorbance) from the beginning of titration until nearly the equivalency point. For a monochromatic spectrometer, one must choose a strongly absorbing wavelength for the chromophore in question. This must be balanced with a wavelength at which the instrument is sufficiently sensitive. The sample should be tested at a wavelength that provides a large range of transmittance values that still allows for accurate measurement by the spectrophotometer.

When a chromophore is added to a solution, the concentration of the chromophore is reduced both over time, by addition of the titrant even if a chemical reaction does not take place (simple dilution if the added titrant volume is large enough). This can easily be observed by adding water to a dye solution. The absorption is reduced without the elimination of the chromophore. To combat this, a sufficient experimental volume must be used with a titrant of sufficient strength such that the necessary titrant volume minimally affects the concentration.

On the spectrophotometer used (Sargent-Welch Model SD) a wavelength of 450 nanometers was chosen for measurement. At this wavelength, both sufficient absorption of the tested chromophore (I_2/I_3^-) is present, the spectrophotometer has sufficient number of interrogating photons, and sufficient linearity and sensitivity of the system is observed.

In order to determine the equivalency point, a 2-part linear regression must be used. The first portion encompasses the major portion of the titration from the beginning of the linear range up to the point just before linearity ceases. The second range encompasses from after the equivalency point until sufficient linearity is achieved. Each of these two linear ranges are independently regressed, and the intersection of the two regions is defined as the equivalency point. A sample graphical representation of this method is shown:

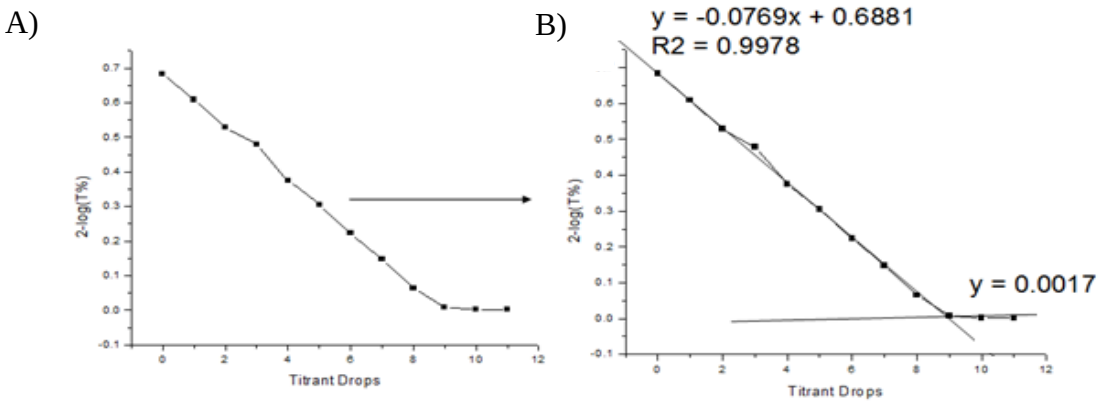

Figure 7: Winkler Titration Equivalency Test. (A) Absorbance data for sample solution as titrant is added. (B) Data is then separated into two linear regions and their intersections calculated as shown. The intersection of the linear regions is a more accurate determination of equivalency point independent of final clarity of solution

The coordinates of the intersection point indicate the equivalency point (the value of the abscissa) and the absorbance value at which this takes place (the value of the ordinate). It is important to note that this method can determine the equivalency point without the dependence on solution clarity or the need to remove all particles from solution. This ordinate value, (unitless) can be converted back into percent transmission using the following relationship:

$$\%T = \frac{\%T_O}{10^A} \quad \textit{Equation 6}$$

This %T calculated value is the value that the spectrophotometer is reading (in %T) at the equivalency point. The slope of the first relationship (during titration) represents the ratio of

absorbance change to quantity of titrant added. The regressed y-intercept value (the offset) should be equaled to the equivalent %T transmission value of the calibrated spectrophotometer before any titrant was added.

Standardization of Sample Measurements

As was stated before, no 'gold standard' exists for oxygen saturation. The easiest way to produce a solution of a given oxygen saturation is to vigorously shake air and water together at a given temperature. An additional factor must be considered for Winkler titration that was ignored for polarimetry – extra oxygen bubbles will add to the measured oxygen concentration. The assumption that water saturated air and air saturated water holds for both Winkler titration and polarimetry, except due to the nature of the different tests, the conclusion of this statement results in different effects on each test. For polarimetry with large area electrodes, net oxygen concentration is measured. As the water and air have equal oxygen tension, bubbles do not significantly affect measurement. In contrast, trapped bubbles before fixation via the Winkler method will continue to react until all oxygen is depleted from solution – both dissolved and extra gas. The addition of extra bubbles that are not dissolved will lead to an excessive apparent measurement of oxygen concentration for a solution under analysis. For this reason it is crucially important to let all gas in solution rise out of solution before testing. Only the dissolved gas should be present.

Standardized Winkler Titration Procedure (Spectrophotometric Addition)

This procedure is a modified version of the original Hach manufacturer's protocol. A total of 60 mL of solution to be analyzed is added to a BOD bottle with great care taken that no bubbles form on the walls or the top of the container. The kit is used as directed up until after the acidification step (just before addition of thiosulfate). A total of 6 mL of solution was placed

into a borosilicate cuvette with a 1 cm path length. This was inserted into a calibrated and zeroed spectrophotometer. An identical cuvette was used as a 100% reference. The cuvette was removed and 20 uL of thiosulfate solution was added and mixed. The solution was then tested again in the spectrophotometer. This process continued until the titration was complete (a few points after equivalency point). Shown below are the transmission and absorbance graphs for an example experimental run.

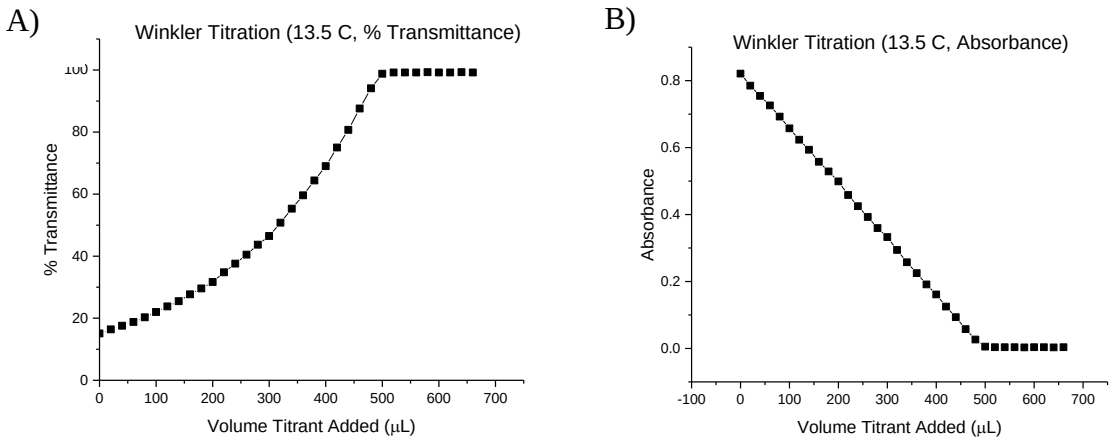

Figure 8: Winkler Transmittance and Absorbance Data. (A) Stepwise Transmission data of sample during Winkler titration. The result is a nonlinear relation with respect to transmittance as expected. (B) Absorbance data for sample solution during Winkler titration. This data was derived from the initial transmittance graph but is easier for interpolation due to its linearity.

Calibration of Winkler Titration Procedure

The relationship between added thiosulfate and dissolved oxygen was determined by mixing air and water at different water temperatures. Full saturation is assumed. After bubbles are dissipated from solution, the temperature is recorded and a Winkler titration is performed. As the saturation concentration of oxygen is known as a relationship of atmospheric pressure and water temperature, multiple values of oxygen saturation can be tested and a regression formed to relate oxygen saturation to thiosulfate volume. The resultant calibration data is shown below.

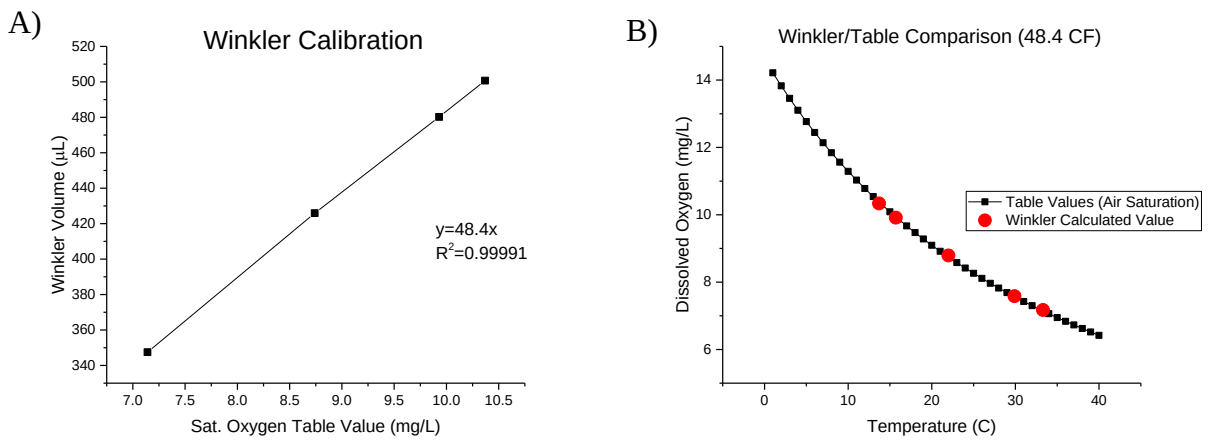

Figure 9: Derivation of Calibration Factor for Winkler Titration. (A) Winkler values for air saturated water show a positive linear correlation with the expected theoretical value. (B) When the calibration factor is applied, the converted Winkler values match closely to the table values over the desired range.

Calculated volumes of titrant for each experiment were then compared to dissolved oxygen (DO) values for air saturated water at the corresponding temperatures. The slope of this graph corresponds to the conversion factor between microliters of titrant and concentration of dissolved oxygen within the solution. The resultant conversion factor: $\frac{\mathbf{48.46}\ \boldsymbol{microliters\ titrant}}{\mathbf{1}\frac{\boldsymbol{mg}}{\boldsymbol{L}}\boldsymbol{dissolved\ oxygen}}$ was used to convert the original volumes calculated through winkler titration into concentrations of dissolved oxygen within the test sample. When the original microliter values are converted with the conversion factor and overlaid onto a water temperature-saturation curve from accepted values, the average error was only 0.39%. This shows internal accuracy in the calibration and suggests that this conversion factor is correlated closely with the behavior of dissolved oxygen in air saturated water.

.

Aqueous Dissolved Oxygen Models

Dissolved Oxygen and Biological Conditions

Typical studies regarding oxygen content within a liquid, are interested in the aqueous dissolved oxygen content contained in a given volume of solution. This value is used to determine the water quality for various wildlife and fish that depend on some form of oxygen supply within the water to survive. Below certain threshold levels, the water cannot sustain populations of aquatic animals and the animals die off as a result. This dissolved oxygen measurement is typically reported in units of mg O_2/Liter of water or PPM (parts per million). A step by step conversion between each unit shows that these two measurements are numerically equivalent assuming standard conditions. Therefore, these units were used interchangeably during the experimental process and results will be referred to using the mg/L notation.

Standardization of Measurement Techniques

Measurement of dissolved oxygen (DO) content with a highly repeatable and accurate reporting proves to be difficult, even within a controlled laboratory environment. Common laboratory and field DO measurements rely on optical/luminescent[23], polarometric, amperometric[24], and titration[25–28] methods to consistently define values and provide more reliable calibration for devices. For our studies, the latter two methods are used. Difficulty in reliable calibration is due to the lack of an exact "gold-standard" for comparison, and inconsistencies in a number of prior published models for numerical interpolation with collected data. When these two problems are combined the issue is magnified and the confidence of high precision, repeatable measurements comes into question.

Table 1: Oxygen Solubility for Distilled Water

Temp (C)	DO (mg/L)	Temp (C)	DO (mg/L)	Temp (C)	DO (mg/L)	Temp (C)	DO (mg/L)	Temp (C)	DO (mg/L)
0	14.62	**6**	12.45	**12**	10.78	**18**	9.47	**24**	8.42
1	14.22	**7**	12.14	**13**	10.54	**19**	9.28	**25**	8.26
2	13.83	**8**	11.84	**14**	10.31	**20**	9.09	**26**	8.11
3	13.46	**9**	11.56	**15**	10.08	**21**	8.91	**27**	7.97
4	13.11	**10**	11.29	**16**	9.87	**22**	8.74	**28**	7.83
5	12.77	**11**	11.03	**17**	9.66	**23**	8.58	**29**	7.69

For fresh water, at sea level, and standard atmospheric pressure, the predicted maximum dissolved oxygen content varies between 14.6 mgO_2/L at 0°C to 7.6 mg O_2/L at 30°C with an error of +/- 0.5 mgO_2/L. Typical values for water under normal conditions are shown in Table: 1. Most modern estimation models report values that confer with this statement. Most modern instruments for DO measurements, can likewise read and report DO values within +/- 1 mgO_2/L following manufacture-described calibration techniques. This calibration requires adjustment (manually in some cases) for temperature and salinity is applied where necessary[29,30]. This constitutes a maximum error of 15.1% at the high end. While this sounds marginally acceptable, the error magnitude continues to increase as the concentration drops at a given temperature. Reduction of variance in the instrument sensing system and model system works to produce more reliable measurements with lower total error. While in many applications, reporting the DO value to the nearest 1 mgO_2/L is acceptable, significant care is necessary to reduce the error to +/-0.1 mgO_2/L and much more care (when even possible) is necessary to reduce the error to

+/-0.01 mgO_2/L. Many digital instruments (including the YSI Model 58 used extensively in this study) display this digit despite an inherent error (applicable in most measuring situations) that is larger than the value contained in the digit.

Even with perfect instrumentation precision sensor and calibration, various practical situations for measurement add potentially significant sources of error. Presence of ions other than oxygen molecules provides interference between device measurements and results in diminished precision of the final value. When under high pressure, as in deep water or other environments, the pressure difference across the membrane in a DO amperometric lead causes the membrane to distend. The thinner membrane allows higher amounts of oxygen to travel across, causing a reading higher than normal. This change in measurement is increased as membrane distension increases. Passive pressure compensation using diaphragms (as used in a number of the YSI 5700 series probes) can combat this, however it requires a larger internal electrolyte chamber which causes additional issues. The larger reservoir size relative to the sensory cell the further the distance any molecule within the electrolyte solution must travel before it can be "used up" by the sensory cell. In more extreme cases, this results in an electrolyte solution that has a non-zero oxygen content and thus more inherent error in the measurement. Therefore, the polarization process for this type of electrode takes longer with increased electrolyte solution.

Dissolved Oxygen Modeling methods:

Assuming no consumption, generation, and a sufficient oxygen supply, aerated water will reach a dissolved oxygen equilibrium value given sufficient time. The magnitude of this equilibrium concentration is a function of oxygen content in aeration gas, gas pressure, and

solution temperature. The magnitude of this oxygen saturation value for a given temperature is predicted by the Bunsen Solubility Coefficient model and Henry's Law:

$$C_{aq} = \frac{K_H(T)}{P_p} \qquad \textit{Equation 7}$$

In the simplified form, C_{aq} is the oxygen concentration in moles, $K_H(T)$ is the Henry's Law constant as a function of temperature for oxygen in water, and P_p is the partial pressure of oxygen in the aeration gas. Since the Henry's law coefficient is a function of temperature [$K_H(T)$], a Van't Hoff relationship can be used to predict the $K_H(T)$ values at a certain temperatures given a Q coefficient (in units of Kelvin), where the Q coefficient is defined as the enthalpy of solution divided by the universal gas constant. In literature this unit is typically referred to as the 'C' or 'K' value, In this report, this value will be referred to as Q for consistency. The relationship is as follows:

$$K_H(T) = K_H(298) \cdot e^{\left[Q \cdot \left(\frac{1}{T} - \frac{1}{298}\right)\right]} \qquad \textit{Equation 8}$$

$$Q = \frac{\Delta_{solv} \cdot H}{R} = -\frac{d\left[\ln\left(K_H(T)\right)\right]}{d\left(\frac{1}{T}\right)} \qquad \textit{Equation 9}$$

Where $K_H(T)$ is the K_H coefficient (in Kelvin) for a given temperature with reference to the standard temperature of 298 K.

From literature the $K_H(298)$ and Q values compiled from contemporary studies vary[31]. Even the best Henry's Law model coefficients fail to accurately predict the oxygen saturation value for water at more extreme temperatures and are therefore only reliable within a small range[32]. Therefore, several alternate numerical approximations have been created over time to predict the numerical value for oxygen saturation[33]. Current models have expanded on the original theory contained in oxygen saturation predictions with some of the more famous models coming through the work of Weiss and Benson. Through the use of more modern techniques and equations, newer models have an absolute error of less than $0.002 mgO_2/L$[34,35] The general idea

behind these models is the fitting of real world data into a modified the Van 't Hoff equation[32]. Fitting coefficients are derived through least-squares analysis. For accurate predictions, both the salinity and differing gas pressure must be considered since they exert a great influence on the final result. These correction factors are semi-independent and can be individually calculated (correction factors of S, P respectively) to form a set of factors that are multiplied by the calculated maximum dissolved oxygen content in fresh water at 1 atm of pressure[34]. This relationship is shown as:

$$DO = DO_o * S * P \quad \textit{Equation 10}$$

Based on these equations, DO curves for oxygen saturated water can be generated for various environmental conditions. Since the values for dissolved oxygen content at saturation are dependent on both temperature and pressure, it is necessary to fix one of the variables while varying the other. The resultant curves based on fixed temperature and fixed pressure are shown below (left and right graph respectively). There is a linear relationship in regards to fixed temperature and varying pressure, however there is a nonlinear relation between fixed pressure and varying temperature.

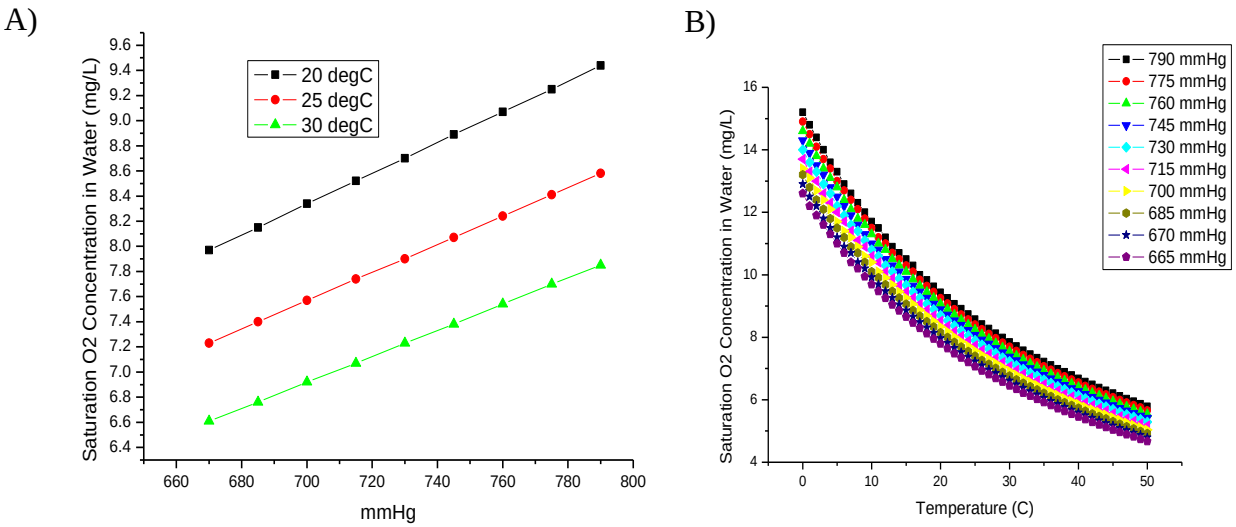

Figure 10: Oxygen Saturated Water Curves Under Various Conditions. (A) Linear relation between oxygen concentration and environmental pressure at fixed temperature. (B) Graphical representation of the nonlinear relation between temperature and oxygen concentration at fixed pressure[78].

Dissolved Oxygen Measurement with Polarometric/Amperometric sensing:

Function of a Clark Electrode

Dissolved oxygen electrochemical sensors typically rely on the Clark electrode design[37,38]. In this design, current flows across a biased electrochemical sensor based on the functional oxygen reduced within the cell reservoir. Variation of the bias voltage in constant oxygen tension and temperature can produce a polarogram plot. However, in typical senor application the bias voltage is fixed and the sensor current is used for oxygen content measurement. Assuming proper maintenance of the device (no leaks, tears, etc.) and sufficient polarization, the internal cell environment can be approximated by an initial value of 0 mg/L of oxygen. Therefore, as oxygen is added to the system, the increase in current is proportional to the DO content of the test solution.

For this type of instrument an electrochemical cell is used with a platinum or gold cathode and a silver/silver chloride reference anode. Historically a toxic a KCl/calomel reference anode was commonly used[39]. A chemical cell of this type uses 0.5-3M KCl solution electrolyte resulting in a sensor life that is limited by the available chloride ions. Additionally, other factors such as silver plating on the noble metal cathode and AgCl plating on the silver anode can lead to eventual failure of the cell. The relationship between electrolyte concentration and temperature for the reference electrode has been shown in some studies with the equation below[40,41].

$$AgCl_{(S)} + e^{-} \Leftrightarrow Ag_{(s)} + Cl^{-}$$

$$E_{Ag/AgCl} = E_O^{Ag/AgCl} - \frac{RT}{1F}\ln Q_{Cl^-} \qquad E_O = .223V \pm 0.13mV @ 25°C$$

$$E_O(t) = 0.23695 - 4.8564x10^{-4} - 3.4205x10^{-6}t^2 - 5.869x10^{-9}t^3$$

where t is in °C from 0°C to 95°C

A thin Teflon® membrane is placed between the measured solution and the cathode and a bias of -0.5 to -0.8V (a noble metal acts as cathode and is negative with respect to the reference) is applied to the cell. Measured current is proportional to the oxygen concentration available to be reduced on the cathode surface. For the electrolyte solution, KCl is preferred over NaCl due to a balance in ionic radius. This permits diffusion of ions to occur at similar rates for a balanced rate between cathode and ion reactions

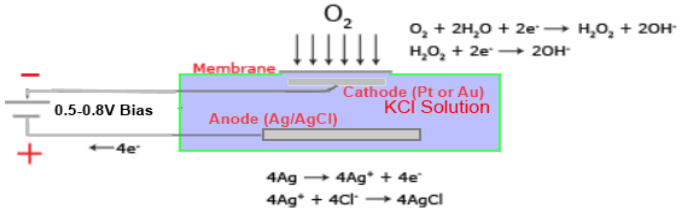

Figure 11: Main Reactions within Clark Electrode. Reactions between the anode and cathode allow flow of ions and measurement of dissolved oxygen concentration[78]

Many of the experiments in this work use a modern YSI type 5739 probe in conjunction with a YSI 57 and YSI 58 meters to take measurement data. Additionally a Milwaukee MW600 DO meter/probe was used.

The current flow through a standard Clark electrode is proportional to the area of the cathode (since it typically has less surface area than anode), membrane diffusivity, and membrane thickness. Modern Clark electrodes use FEP (Teflon®) membranes of 0.5 to 2 mil (13 to 50 microns) thickness. Directly behind (and touching) this membrane is a noble metal cathode in a KCl solution. Further back from this membrane in the well of the sensor is an Ag/AgCl reference anode.

Many devices such as the MW600 and YSI 58 models, recommend at least a two point calibration of the system. The suggested points are one at a "zero" point and another as a saturated water sample at the experimental temperature. For a two point calibration dissolved oxygen meter, the measurement reading is a function of a linear calibration between current and dissolved oxygen value:

$$DO(P,T)[mgO_2 / L] = (Gain) \cdot (Current) + (Offset) \quad \textit{Equation 11}$$

Where the values of Gain and Offset are used to map the measured sensor current value to the reported oxygen concentration. When the sensor has no current, the offset value is adjusted to null (0) to correct the instrument. As long as the environmental factors are unaffected (temperature and pressure) sensor bias voltage is maintained at a constant value and thus, the current measured is linearly proportional to oxygen concentration.

The constants for A and B are solved through linear least squares regression.

The result is a linear expression that can predict the measured values as a function of temperature. The Dissolved Oxygen Compensation Factor (DOCF) can be calculated for each degree C using the regressed coefficients.

While this is noteworthy, it does not get us closer to correcting the measurement error. From prior studies, it has been noted that an approximately 5% error exists per degree (in Celsius) difference from the calibration point for an amperometric DO sensor[38]. After internal correction a systemic error exists, but it is far overweighed by random experimental error

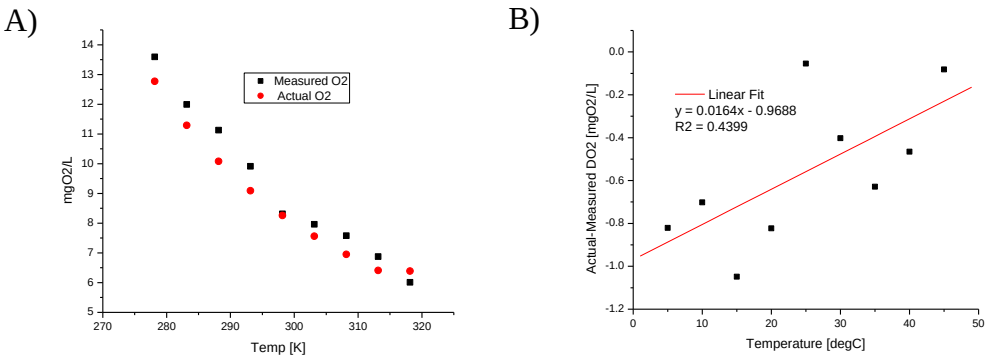

Figure 12: Internal Temperature Compensation within Probe Device. (A) When measurements are taken at values close to calibration temperature, only small amounts of error are present. (B) As the probe is used in temperatures much different from its calibration temp, errors increase and only a weak correlation is shown

From the regression, a weak temperature correlation exists between the predicted and measured values. From the slope, this appears to be around 1.5% per degree Celsius. Inherent measurement correction is non-trivial as multiple systems are non-linear. To offset the role of temperature on the membrane permeability a thermistor is used in the sensor probe to feed the data into computer (analog or digital) to process the correction factor. For the older YSI instruments, analog computers based on single or multiple operational amplifiers (Op-Amps) were used.

Calibration methods for Amperometric sensors:

The lack of a 'gold standard' reference model for oxygen complicates the process of calibrating Clark electrode sensors. In comparison, when calibrating a pH electrode, buffer solutions of various known pH values are available and long lived when properly stored. This is not the case for dissolved oxygen, small deviations in temperature cause changes for the solution oxygen content.

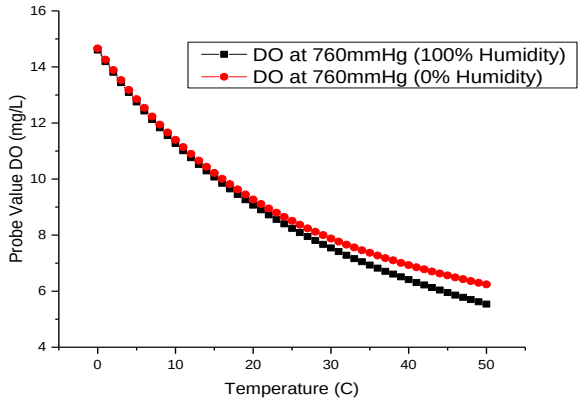

Figure 12: Variance in Probe Values Due to Humidity. The probe shows a slight variance when exposed to 100% vs 0 % humidity. This deviance grows larger as the temperature increases.

Therefore, several assumptions must be made to provide a standard with which to calibrate the device against and test measurement data. The assumptions chosen for this set of experiments were as follows:

1) Air saturated water has the same oxygen content as fully water saturated air
2) The humidity of water saturated air affects the oxygen content.
3) Vigorous sustained shaking of air in water saturates the water at the given temperature (measured at end of shaking in case of slight elevation)
4) This water saturation persists long enough to allow measurement of sample

5) If water is saturated at a given temperature and the temperature lowers, the water will be unsaturated at the new temperature even if no oxygen is removed from solution, conversely, if the saturated water is heated, it will become oversaturated and eventually will lose O_2 from solution.
6) Oxygen content of the solution is dependent on the aerating gas partial pressure (of oxygen)
7) The addition of sodium bisulfate can scavenge oxygen from solution – a tiny amount of cobalt chloride can boost the effect[50]
8) Even without stirring, if left open to the atmosphere, over or under saturated solutions will tend towards equilibrium with air.
9) The barometric pressure is necessary for probe calibration
10) Additionally, if open air (air not fully saturated with water) calibration is used, air humidity information is also necessary for accurate compensation.
11) For long duration experiments, current output of the Clark electrode decreases over time. This change must be accounted for via frequent calibrations back at the calibration point.

In addition to these assumptions there are a number of practical considerations to account for. This list of practical considerations must also be considered for proper measurements:

1) The probe must reach thermal equilibrium and polarization before calibration begins. If the probe has thermal compensation, the compensator and cell temperatures must come into agreement. This is especially true for the YSI 5700 series probes.

2) Care must be observed to prevent water droplets from forming or being transferred to the membrane.
3) Water saturated air has a lower thermal conductivity than water, therefore, probe thermal equalization takes longer in water saturated air over air saturated water.
4) Water saturated air must be fully saturated (RH=100%) for this technique to work. Humidity can affect sensor calibration.
5) While water saturated air is a manufacturer preferred technique[46], in practice, thermal errors can far outweigh other error sources in comparison to air saturated water.
6) Winkler titration is minimally affected by temperature and humidity and can thus be used as more reliable comparison
7) Spectrophotometric alterations to Winkler method reduce inherent error of measurement
8) The instrument should be calibrated at the same temperature it will be used to measure at, relying as little on thermal correction as possible.

For the experimental studies, the following standardized calibration procedure was used for measurements at or around room temperature:

1) Adjust sensor zero point per manufacture specifications
2) Polarize measurement sensor for at least 15 minutes.
3) Place 350 ml of deionized water in a 500 mL glass mason jar at room temperature
4) Heavily shake jar for 30 seconds. Shake jar a second time after the bubbles from the first shaking began to disappear.
5) Place sensor probe into mason jar and record temperature recorded (A separate K-type thermocouple thermometer was also used for redundancy.

6) Rapidly swirl electrode in solution taking care not to bump the jar walls. Note: YSI cathode has larger area and is thus more susceptible to measurement error due to stagnant water in front of the probe surface. With sufficient swirling, the measured value will stay steady to permit reading.
7) Adjust calibration factor to the proper level.
8) Store sensor in a 100% humidity storage bottle between measurements in the vertical position. Instrument is left on for the entire study.
9) Check probe measurements against reference solution often to compensate for probe drift over time

For measurement the following procedure is used:

1) Calibrate probe at temperature close to experimental temperature
1) Remove sensor probe from storage container and place into solution and let sit for 2-5 min to allow for thermal equilibrium. This can be monitored via probe internal temperature reading
2) Swirl sensor probe and record DO value and temperature once measurement has stabilized
3) Remove sensor from solution, rinse if necessary, dry, and place back into storage container in vertical position

Oxygen Delivery Via Nanobubbles

Nanobubbles and Lipoaspirate Solutions

To study the effects of micro/nanobubbles on tissue samples we tested using a microbubble generator and lipoaspirate sample acquired through patient consent. The sample was divided into two separate categories: “macrofat”, and “nanofat” samples. Each experimental group also

had a corresponding control for a total of four groups. The macrofat samples were defined as 50 ccs of lipaspirate sample that was subjected to 3 washes with PBS before the trial began. No additional processing was done at this time.

The nanofat sample procedure was derived from a paper from the Tonnard lab[51]. In this paper, the lab group demonstrated an increased removal of oils and an improvement in regenerative effects over time when fat was subjected to shear forces prior to reinjection. In their studies, the passed the lipoaspirate sample 20 times between interconnected (via Luorlock) syringes. Through this process, the sample is broken up into smaller pieces. Additionally, the sample can also be passed through a secondary filter after syringe processing to remove additional oils from the tissue. For our tests, we performed the same procedure as was described in the Tonnard paper to create a nanofat sample for experiments. A nanofat sample was defined as 50 ccs of lipoaspirate that had been washed, and then passed through two interconnected, 10 cc syringes at least 20 times and then filtered using a 0.5 mm mesh filter.

Preparation of Incubation solutions

Approximately 250 mL of PBS solution (location, order etc) was used for incubation during each trial. Control solutions were standard sterile PBS that had been aliquoted for each test. Microbubble solutions were created using the microbubble generator illustrated in Figure 2. Experimental (Microbubble) solutions were composed of sterile PBS solutions that had been exposed to microbubble generation for 10 minute duration. Incubation solution was then poured into a separate container that had 50 ccs of lipoaspirate (either macrofat or nanofat versions). Oxygen content was then measured by using a standard Clark electrode (MW600) to test the content of the liquid solution over time. The results of this experiment are shown below.

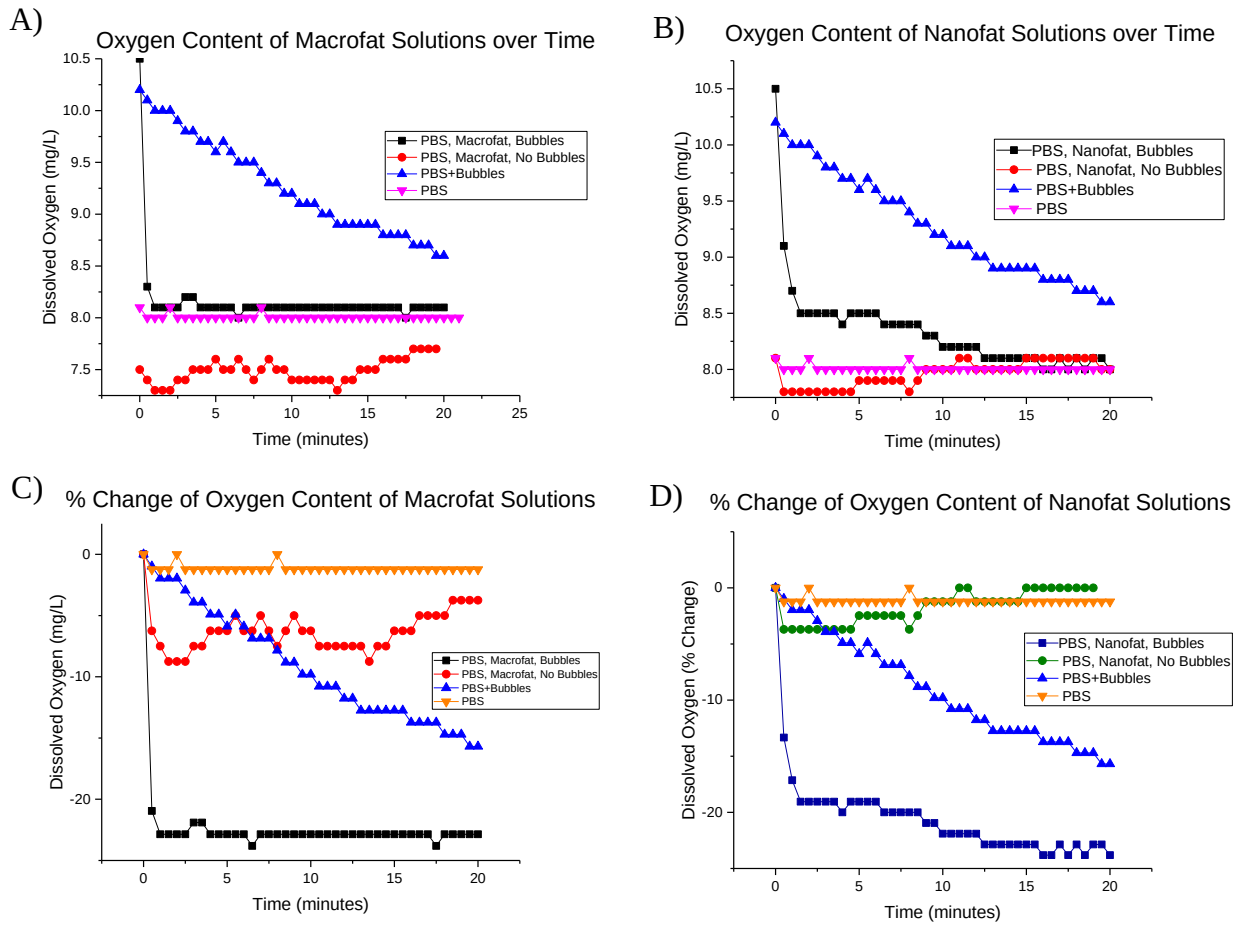

Figure 14: Oxygen Content of Lipoaspirate Solutions. (A)Macrofat solutions showed a rapid decrease in oxygen content immediately after mixing. (B)Nanofat solutions showed a similar decrease but this decrease was not as dramatic as seen in the macrofat data. The percent change of each solution is illustrated in (C) and (D) respectively.

When lipoaspirate samples were incubated in PBS solutions, they caused an immediate decrease in the dissolved oxygen content of the liquid. Macrofat samples showed a large decrease that went below the baseline DO content of PBS. When exposed to microbubbled solution, these samples continued to show a rapid decrease in DO content below baseline levels. The behavior of this system suggests that the macrofat tissue is oxygen starved and will uptake additional amounts of oxygen when given a large enough supply. Nanofat solutions showed a similar decrease in oxygen content, however, the decrease was not as significant as the macrofat

solutions. The decrease of oxygen from solution in this case was still maintained above baseline levels for a duration of approximately twenty minutes. This coincides with previous research, in which we have found that the shearing technique for generating nanofat causes a decrease in the viable cells within the mixture. Since there are less viable cells in the nanofat mixture, there is less demand for oxygen within the tissue, leading to a less pronounced decrease in oxygen content. The results of this experiment suggest a link between the oxygen drop in solution and the presence of cells (tissue). The experiment showed a larger decrease when more cells were present (macrofat sample) compared to when less cells were present (nanofat sample).

Gas Production in Yeast Model

Based on the previous studies, it was not clear whether the gas contained within a microbubble was ever released into the surrounding environment. The lipoaspirate studies mentioned in this thesis suggested that some mechanism occurred during transfer. However, the decay in measurable dissolved oxygen content was immediate and drastic in response when combined with lipoaspirate samples. This could be explained under a couple scenarios, either the microbubbles were rapidly destroyed due to transfer, or the contents of microbubbles were dispersed into the environment (and theoretically the tissue). Therefore, it was necessary to test in another model system to determine whether the decay of oxygen in solution was due to rapid destruction of microbubbles upon transfer, or the dispersal of gas contents into the liquid. A yeast model was chosen as an alternate experimental system of study.

Measurement of Gas Production from Yeast Solutions

For this experiment, the displacement of water within a closed system was used as a measurement of the gas produced. The summarized experimental procedure follows:

DI water was warmed until it reached the appropriate temperature (110 F) to ensure proper environment for yeast.

While waiting for water to reach appropriate temperature, 200 mL DI water was added to a separate container (container max volume approximately 400 mL)

A graduated cylinder was completely filled to capacity with an additional supply of DI water (to top)

The cylinder was covered with flat glass and quickly inverted into the 400 mL container, glass top was removed from cylinder once cylinder submerged and inverted under water

Ran one end of tubing through rubber stopper and other end inside of the inverted graduated cylinder

Added 2.25 teaspoons (~11.09 mL) of Fleischmann's Active Dry Yeast to 250mL flask

Extracted 0.5 cup from warm water (110 F), and added to flask

Stirred yeast+water mixture for 10 seconds

Placed rubber stopper with tubing on top of flask to seal container

Took images of cylinder every 30 seconds for 25 minutes

For analysis, Images were transferred into Image J, and the water level was measured for each picture.

<u>Experimental (microbubble) procedure variation</u>

Same as control except bubbled DI water was added to yeast instead of standard DI water

Bubbled water sample was created using microbubble generator (generator function and properties detailed in this report) for 5 minutes on DI water sample. This microbubbled water sample was then added to yeast when needed.

Measurement of Flow Rate and Total Gas Production:

After measurement of gas volume at each time point, 2 numbers were calculated from the data set: flow rate of gas, and total gas produced at each time point. The flow rate of gas was calculated as the change in gas volume over each interval (in mL/min)

$$\boldsymbol{Flow\ Rate} = \frac{\boldsymbol{V_t - V_{t-1}}}{\boldsymbol{t_i - t_{i-1}}} = \frac{\boldsymbol{\Delta Vol}}{\boldsymbol{\Delta t}}, \text{ where t[min],vol[mL]} \qquad \textit{Equation 12}$$

Total gas production was calculated as the summation of gas that had been collected up to that time point. Due to the nature of the experiment, this summation can be simplified into the following equation:

$$\boldsymbol{Total\ Gas\ Production} = \boldsymbol{V_t - V_{initial}} \qquad \textit{Equation 13}$$

For each trial of this gas production experiment, the microbubble/yeast solution produced a larger volume of gas than the control case

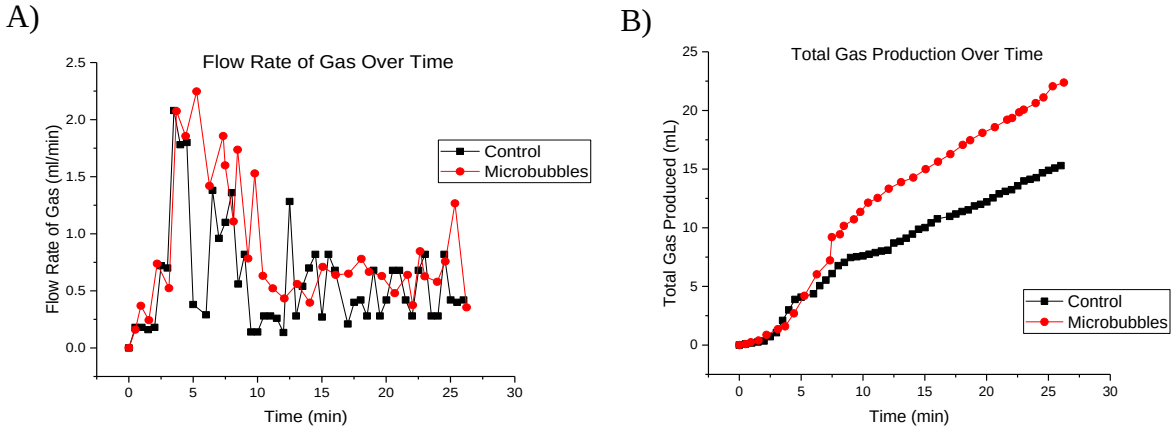

Figure 15: Gas Production in Yeast Model. Spikes in gas flow rate (A) show deviances in the gas production between the two sample types. When the volume is summed in (B) the microbubble solution exhibits a higher volume of gas production.

As seen in Figure 15 the Microbubble +Yeast mixture had occasional spikes in its gas flow rate which were higher than the flow rates within the control case. These differences add up over time and caused a large deviation in collected gas volumes after 25 minute duration. After 25 minutes the final gas volumes deviated by 48.1% with the microbubble solution reaching the higher value, (22.06 mL and 14.89 mL volumes respectively). This system behavior is indicative of some form of microbubble action within the system. Since gas could only enter the system through the release of microbubbles or additional gas production from the yeast due to exposure to microbubbled solution. Based on previous studies, the microbubbles reached an additional saturation point 24% higher in oxygen content than control. Since the additional gas collected during from the microbubble+yeast solution is much higher than this (twice the predicted value), it is most likely that the yeast had an increased response to the micro/nanobubbles in solution to account for the difference from theoretical and experimental value. However, it is unclear whether the gas produced from the system is entirely due to yeast production or more likely, the combination of microbubble released contents and an increased metabolic rate within the yeast sample.

Conclusions/Future Considerations

Future Work:

Visualization of Oxygen Delivery into Tissue (DHE Assay)

Although the incubation data suggested delivery of oxygen into tissue, it will be necessary to prove that the oxygen is able to enter the tissue rather than simply forced back into the atmosphere. For this experiment, 50 ccs of tissue will be separated into experimental groups. To ensure the greatest probability of success the nanofat procedure will be used to generate the experimental sample. Once processed, the nanofat samples will be incubated in either

microbubbled solution (10 min generation time) or control (sterile PBS stock solution) for 20 minutes. After the incubation period, the tissue will be microsectioned into three pieces at 0, 10, 20, 1 hour after incubation. Each piece will then be stained with dihydroethidium and imaged under a microscope to show the oxygen levels within the tissue.

Dihydroethidium (DHE) was chosen to visualize the presence of oxygen within tissue. Under hypoxic conditions, superoxide levels surrounding the cells grow rapidly leading to a much higher concentration of the molecule than under standard oxygen conditions. The compound DHE reacts with the superoxide to form a complex that when combined with a fluorochrome allows for visualization of the superoxide-DHE complex. Normoxic tissue contains minimal levels of the superoxide ion in the local region. Since hypoxic tissue contains more superoxide ions, it produces more superoxide-DHE complexes when stained via chemical assay. This leads to a higher fluorescent intensity when visualized under the microscope. However, due to the non-stoichiometric nature of the reaction, each assay shows a relative comparison that demonstrates which tissue exhibits higher levels of the superoxide ion and is thus more hypoxic.

Use of Microbubbles for Irrigation of Tissue:

Microbubbles are negatively charged spheres that can persist within a solution. When microbubbles are present in sufficiently high concentrations they act as a cleaning mechanism. As the bubbles flow around the environment they bump into particles and sediment. Due to ionic charges surrounding the shell of the microbubble, they also attract and collect particles as they flow through the region. When the bubbles dissipate, they cause the attached particles to aggregate in solution. This acts as a flocculation process that separates the solution into a variety of particles dependent on density. This process is already in use in environmental reclamation

projects to separate particles so that they can be filtered more easily from water. Therefore, a microbubble solution could be used to clean out a wound more efficiently than the standard treatment. Additionally, the solution could be combined with an antiseptic wash to not only clean the wound, but remove additional bacteria.

Improvement of Adipose Tissue Grafting

We believe that the additional oxygen supply as provided by microbubbles is sufficient to increase oxygen content of a tissue graft. This increased oxygen supply allows for a higher survival rate of cells within the tissue which leads to a higher retained volume over time. This effect also has the possibility to increase the maximum size of a grafted bolus due to increased diffusion limits. Our lab currently looks to apply this method in an in-vivo system to see if the properties are sufficient to improve retention.

Enrichment of Cell Matrix and Scaffolds

Recent studies have attempted to design artificial matrices to replace such organs like the human ear. However, several methods fail due to increased contraction and apoptosis of cells over time. It is possible that this case has a similar problem in that the cells do not have a sufficient oxygen or nutrient supply to fulfill their needs and die off as a result. If we can supply an additional source of nutrients that is persistent through the development process, the matrix survival should improve and the scaffold should retain more of its intended characteristics. This would allow a more efficient grafting process.

Conclusions:

We were able to create a simple device that infuses gas microbubbles into a liquid solution. These bubbles are on the order of 40 microns in diameter initially but shrink to around 2 microns after some period of time. These bubbles persist in solution and serve as an additional reservoir

of gas available over time. When exposed to an object that contains a lower partial pressure of the gas, the bubbles deliver their contents into the tissue, raising the local partial pressure of the gas. Using this property, we were able to use microbubbles as a delivery mechanism to transport an additional oxygen supply to a tissue sample. We first showed a marked decrease in dissolved oxygen content when a tissue sample was present, which suggested a need for higher oxygen levels within the tissue. This hypothesis was confirmed via DHE staining, which showed that tissue incubated in a solution containing oxygen microbubbles exhibited lower levels of the superoxide ion, suggesting less hypoxic conditions. Based on the results of these studies, microbubbles are an alternative method for delivering oxygen into a local tissue supply.

References:

1. Khouri RK, Khouri R-ER, Lujan-Hernandez JR, Khouri KR, Lancerotto L, Orgill DP. Diffusion and perfusion: the keys to fat grafting. *Plast Reconstr surgery Glob open*. 2014;2(9):e220. doi:10.1097/GOX.0000000000000183.

2. Hopf HW, Gibson JJ, Angeles AP, et al. Hyperoxia and angiogenesis. *Wound Repair Regen*. 2005;13(6):558-564. doi:10.1111/j.1524-475X.2005.00078.x.

3. Khouri RK, Rigotti G, Cardoso E, Khouri RK, Biggs TM. Megavolume Autologous Fat Transfer. *Plast Reconstr Surg*. 2014;133(3):550-557. doi:10.1097/01.prs.0000438044.06387.2a.

4. Hideki T. *Micro- and Nanobubbles Fundamentals and Applications*. Boca Raton, Florida: Pan Stanford Publishing; 2015.

5. Petsev ND, Shell MS, Leal LG. Dynamic equilibrium explanation for nanobubbles' unusual temperature and saturation dependence. *Phys Rev*. 2013;88.

6. Attard P. The stability of nanobubbles. *Eur Phys J Spec Top*.:1-22.

7. Li P, Takahashi M, Chiba K. Degradation of phenol by the collapse of microbubbles. *Chemosphere*. 2009;75:1371-1375.

8. Takahashi M, Chiba K, Li P. Free radical generation from collapsing microbubles in the absence of a dynamic stimulus. *J Phys Chem*. 2007;111:1343-1347.

9. Takahashi M, Chiba K, Li P. Formation of hydroxyl-radicals by collapsing ozone microbubbles under strongly acidic conditions. *J Phys Chem B*. 2007;111:11443-11446.

10. Zaneti R, Etchepare R, Rubio J. Car wash wastewater reclamation. Full-scale application and upcoming features. *Resour Conserv Recycl*. 2011;55:953-959.

11. Miyamoto M. *Abstracts of MRS Meeting*.; 2006.

12. Miyamoto M. Degreasing of solid surfaces by microbubble cleaning. *Jpn J Appl Phys*. 2007;46:1236.

13. Watabe T, Matsuyama K, Takahashi T, Matsuyama H. Use of microbubbles to reduce membrane fouling during water filtration. *Desalin Water Treat*. 2014:1-7.

14. Ohnari H. Effect of microbubble bathing of lower extremities on peripheral circulation. 2010:25-32.

15. Ebina K, Shi K, Hirao M, et al. Oxygen and air nanobubble water solution promote the growth of plants, fishes, and mice. *PLoS One*. 2013;8(6):e65339. doi:10.1371/journal.pone.0065339.

16. Carpenter JH. The Accuracy of the Winkler Method for Dissolved Oxygen Analysis. *Limnol Oceanogr*. 1965;10(1):135-140.

17. Strickland JDH, Parsons TR. A Practical Handbook of Seawater Analysis. *Fish Res Board Canada, Bull*. 1972:71-75. http://scholar.google.com/scholar?hl=en&btnG=Search&q=intitle:A+PRACTICAL+HANDBOOK+OF+SEAWATER+ANALYSIS#0.

18. Allee W., Oesting R. A Critical Examination of Winkler's Method for Determining Dissolved Oxygen in Respiration Studies with Aquatic Animals. *Physiol Zool*. 1934;7(4):509-541.

19. Beadle LC. Measurement of Dissolved Oxygen in Swamp Waters. Further Modification of the Winkler Method. *J Exp Biol*. 1958;35:556-566.

20. Carvalho AD, Calado J, Moura M. Spectrophotometric Determination of Dissolved Oxygen in Demineralized Water. *Rev Port Quim*. 1963;5(1):15.

21. Broenkow WW, Cline JD. Colorimetric Determination Of Dissolved Oxygen At Low Concentrations. *Limnol Oceanogr*. 1969;14(3):450-454.
22. Swinehart DF. The Beer-Lambert Law. *J Chem Educ*. 1962;39(7):333-335.
23. Glazer BT, Marsh AG, Stierhoff K, Luther GW. The dynamic response of optical oxygen sensors and voltammetric electrodes to temporal changes in dissolved oxygen concentrations. *Anal Chim Acta*. 2004;518:93-100. doi:10.1016/j.aca.2004.05.040.
24. Carritt DE, Kanwisher JW. An Electrode System for Measuring Dissolved Oxygen. *Anal Chem*. 1959;31(1):5-9.
25. Montgomery HA., Thom NS, Cockburn A. Determination of dissolved oxygen by the Winkler method and the solubility of oxygen in pure water and sea water. 1964;14(7):280-296.
26. Wilde F. National Field Manual for the Collection of Water-Quality Data. *US Geol Surv Tech Water-Resources Investig*. 1998;book 9(chapter 6).
27. Culberson CH, Knapp G, Williams RT, Zemlyak F. *A Comparison of Methods for the Determination of Dissolved Oxygen in Seawater*.; 1991.
28. Knapp GP, Stalcup MC, Stanley RJ. *Dissolved Oxygen Measurements in Sea Water at the Woods Hole Oceanographic Institution*.; 1989.
29. Fofonoff NP. Physical Properties of Seawater:' A New Salinity Scale and Equation of State for Seawater. *J Geophys Res*. 1985;90(C2):3332-3342.
30. Lewis EL, Perkin RG. The Practical Salinity Scale 1978: conversion of existing data. *Deep Sea Res*. 1981;28(4):307-328.
31. Sander R. Compilation of Henry' s Law Constants for Inorganic and Organic Species of Potential Importance in Environmental Chemistry. 1999;(3).
32. Scott RL, Hildebrand JH. *The Solubility of Nonelectrolytes*. Vol 3rd ed. New York: Reinhold Pub. Corp; 1950.
33. Tromans D. Temperature and pressure dependent solubility of oxygen in water: a thermodynamic analysis. *Hydrometallurgy*. 1998;48:327-342.
34. *U.S. Geological Survey, Change to Solubility Equations for Oxygen in Water*.; 2011.
35. García HE, Gordon LI. Oxygen solubility in seawater: Better fitting equations. *Limnol Oceanogr*. 1992;37(6):1307-1312. doi:10.4319/lo.1992.37.6.1307.
36. Benson BB, Krause D. The concentration and isotopic fractionation of oxygen dissolved in freshwater and seawater in equilibrium with the atmosphere. *Limnol Oceanogr*. 1984;29(3):620-632. doi:10.4319/lo.1984.29.3.0620.
37. Clarke EC., Glew DN. Evaluation of Thermodynamic Functions from Equilibrium Constants. *Trans Faraday Soc*. 1966;62:539-547.
38. Kanwisher J. Polarographic Oxygen Electrode. *Limnol Oceanogr*. 1959;4(2):210-217.
39. Clark L, Wolf R, Granger D, Taylor Z. Continuous recording of blood oxygen tensions by polarography. *J Appl Physiol*. 1953;6(3):189-193. http://www.ncbi.nlm.nih.gov/pubmed/13096460.
40. Bates RG, Bower VE. Standard potential of the silver-silver-chloride electrode from 0 to 95 C and the thermodynamic properties of dilute hydrochloric acid solutions. *J Res Natl Bur Stand (1934)*. 1954;53(5):283-290. doi:10.6028/jres.053.037.
41. Bates RG, Macaskill JB. Standard potential of the silver-silver chloride electrode. *Pure Appl Chem*. 1978;50:1701-1706. doi:10.1351/pac197850111701.

42. Horwitz O. Experimental studies of intramyocardial oxygen tension: increases consequent on breathing pure oxygen in normal hearts and at the borders of ischaemic areas. *J Clin Invest*. 1950;29(6):823. doi:10.1172/JCI34653.
43. Tobias JM, Retondo N. Syringe Oxygen Cathode for Measurement of Oxygen Tension in Solution and in Respiratory Gases. *Rev Sci Instrum*. 1949;20(7):519-523. doi:10.1063/1.1741587.
44. Manole A, Neacsu I, Apostu M-O, Melnig V. Membrane Covered Polarographic Oxygen Sensor Manufacturing Theoretical Considerations. *Analele Stiint Ale Univ*. 2006;(11):25-34.
45. Wise RR, Naylor AW. Calibration and use of a Clark-type oxygen electrode from 5 to 45 degrees C. *Anal Biochem*. 1985;146:260-264. doi:10.1016/0003-2697(85)90424-5.
46. YSI Incorporated. Ysi 58 Operations Manual. 1999.
47. Steinhart JS, Hart SR. Calibration curves for thermistors. *Deep Sea Res Oceanogr Abstr*. 1968;15:497-503. doi:10.1016/0011-7471(68)90057-0.
48. Mawire A. A simple experiment to determine the characteristics of an NTC thermistor for low-temperature measurement applications. *Eur J Phys*. 2012;33(5):1135-1145. doi:10.1088/0143-0807/33/5/1135.
49. Pijanowski BS. Salinity Corrections for Dissolved Oxygen Measurements. *Environ Sci Technol*. 1973;7(10):957-958.
50. YSI Incorporated. The Dissolved Oxygen Handbook. 2009;September.
51. Tonnard P, Verpaele A, Peeters G, Hamdi M, Cornelissen M, Declercq H. Nanofat Grafting: Basic Research and Clinical Applications. *Plast Reconstr Surg*. 2013;132(4):1017-1026. doi:10.1097/PRS.0b013e31829fe1b0.
52. Auten RL, Davis JM. The Role of Oxygen in Health and Disease - A Series of Reviews Oxygen Toxicity and Reactive Oxygen Species : The Devil Is in the Details. *Pediatr Res*. 2009;66(2):121-127.
53. Benson BB, Krause D. The concentration and isotopic fractionation of gases dissolved in freshwater in equilibrium with the atmosphere. *Limnol Oceanogr*. 1980;25(4):662-671.
54. Bishop A. Role of oxygen in wound healing. *J Wound Care*. 2008;17(17):399-403.
55. Carpenter JH. The Chesapeake Bay Institute Technique for the Winkler Dissolved Oxygen Method. *Limnol Oceanogr*. 1965;10(1):141-143.
56. Culberson CH, Knapp G, Williams RT, Zemlyak F. *A Comparison of Methods for the Determination of Dissolved Oxygen in Seawater*.; 1991.
57. Douabul AA, Riley JP. The solubility of gases in distilled water and seawater—V. hydrogen sulphide. *Deep Sea Res Part A Oceanogr Res Pap*. 1979;26(3):259-268. doi:10.1016/0198-0149(79)90023-2.
58. Fridovich I. OXYGEN TOXICITY : A RADICAL EXPLANATION. *J Exp Biol*. 1998;201:1203-1209.
59. Goossens GH, Blaak EE. Adipose tissue oxygen tension: implications for chronic metabolic and inflammatory diseases. *Curr Opin Clin Nutr Metab Care*. 2012;15(6):539-546. doi:10.1097/MCO.0b013e328358fa87.
60. Guo S, Dipietro L a. Factors affecting wound healing. *J Dent Res*. 2010;89(3):219-229. doi:10.1177/0022034509359125.
61. Hodson L. Adipose tissue oxygenation. *Landes Biosci*. 2014;(March):75-80.

62. Kato H, Araki J, Doi K, et al. Normobaric hyperoxygenation enhances initial survival, regeneration, and final retention in fat grafting. *Plast Reconstr Surg*. 2014;134(5):951-959. doi:10.1097/PRS.0000000000000600.
63. Knapp GP, Stalcup MC, Stanley RJ. *Dissolved Oxygen Measurements in Sea Water at the Woods Hole Oceanographic Institution*.; 1989.
64. Lecoultre V, Tam CS. Letter by Lecoultre and Tam regarding article, "Increased adipose tissue oxygen tension in obese compared with lean men is accompanied by insulin resistance, impaired adipose tissue capillarization, and inflammation". *Circulation*. 2012;125(4):e315; author reply e316. doi:10.1161/CIRCULATIONAHA.111.050286.
65. Liu S, Oshita S, Makino Y. Reactive oxygen species induced by water containing nano-bubbles and its role in the improvement of barley seed germination. In: *4th Micro and Nano Flows Conference*. Vol ; 2014:1-8.
66. Matsuki N, Ichiba S, Ishikawa T, et al. Blood oxygenation using microbubble suspensions. *Eur Biophys J*. 2012;41(6):571-578. doi:10.1007/s00249-012-0811-y.
67. Matsuki N, Ishikawa T, Ichiba S, Shiba N, Ujike Y, Yamaguchi T. Oxygen supersaturated fluid using fine micro / nanobubbles. *Int J Nanomedicine*. 2014;9:4495-4505.
68. Montgomery HAC, Thom NS, Cockburn A. Determination of dissolved oxygen by the Winkler method and the solubility of oxygen in pure water and sea water. 1964;14(7):280-296.
69. Morelle R. Shrinking Ship Bubbles could Counteract Climate Change. *BBC News*. 2014.
70. Park J. Oxygen Concentration Microgradients for Cell Culture. 2010.
71. Sherwood JE, Stagnitti F, Kokkinn MJ. Dissolved oxygen concentrations in hypersaline waters. *Limnol Oceanogr*. 1991;36(2):235-250.
72. Sun L, Wolferts G, Veltkamp R. Oxygen therapy does not increase production and damage induced by reactive oxygen species in focal cerebral ischemia. *Neurosci Lett*. 2014;577:1-5. doi:10.1016/j.neulet.2014.05.060.
73. Truesdale GA, Downing AL. Solubility of Oxygen in Water. *Nature*. 1954;173:1236.
74. Weiss RF. The solubility of nitrogen, oxygen and argon in water and seawater. *Deep Sea Res Oceanogr Abstr*. 1970;17(4):721-735. doi:10.1016/0011-7471(70)90037-9.
75. Xu J. Cellular Oxygen Toxicity. OXIDANT INJURY WITHOUT APOPTOSIS. *J Biol Chem*. 1996;271(25):15182-15186. doi:10.1074/jbc.271.25.15182.
76. Yoshimura K, Eto H, Kato H, Doi K, Aoi N. manipulation of stem cells for adipose tissue repair / reconstruction. *Regen Med*. 2011;6(6):33-41.
77. Milwaukee Instruments. MW600 Standard Portable Dissolved Oxygen Meter. *http://www.milwaukeeinstruments.com/site/products/products/standardportable-meters/87-products-g-standard-portable-meters-g-mw600*. 2014.
78. Klopfer, M. Micro and Nanobubbles for Wound Healing Applications. Diss. U of California, Irvine, 2015. Print.